Chemical Engineering Journal 416 (2021) 127697

Contents lists available at ScienceDirect

Chemical Engineering Journal

journal homepage: www.elsevier.com/locate/cej

Flexible nanostructured potassium-ion batteries

Sheng-Bor Huang [1], Yi-Yen Hsieh [1], Kuan-Ting Chen, Hsing-Yu Tuan *

Department of Chemical Engineering, National Tsing Hua University, Hsinchu 30013, Taiwan

ARTICLE INFO

Keywords:
Potassium ion
Flexible
Nanostructures
Nanowires
Phosphide
Storage

ABSTRACT

We describe a flexible and freestanding potassium-ion battery consisted of a bilayer-copper phosphide/copper nanowires (CuP_2/Cu NWs) anode and perylene-3,4,9,10-tetracarboxylic dianhydride/carbon nanotubes (PTCDA@CNTs) cathode with superior rate capability and cyclability to simultaneously achieve fast K^+-insertion/releasing and long shelf life on flexible-based electrodes. The extraordinary rate performance of anode and cathode deliver remarkable capacities of 90 mA h g^{-1} at 12,000 mA g^{-1} and 113 mA h g^{-1} at 5250 mA g^{-1}, respectively. Furthermore, coin-typed full cell exhibits superior charging capacities of 117.3 mAh g^{-1} at 12,000 mA g^{-1} and the good retention (80% after 842 cycles at 400 mA g^{-1}). The energy density in the high-power density region, especially the specific energy density under high power density ($>10^4$ Wkg^{-1}) displayed the better rate-capability retention compared with that of reported literatures of full cells (based on the total mass of anode and cathode). Considering the flexibility and stability, the pouch batteries examined by a bending test maintained ultra-stable open circuit voltage after 5000 cycles with a bending radius of 1.2 cm. Expectedly, the state-of-art nano-engineering design and excellent performance demonstrate the direction and opportunities to further improve the energy density and safety under ultrahigh reaction rates of the wearable potassium-ion batteries.

1. Introduction

Lithium-ion batteries (LIBs) are the dominating power sources of portable electronics with the increasing demands for renewable energy storage. Nevertheless, the common facing challenging for LIBs is the restricted resources of lithium metal compared to sodium, potassium, and calcium metals. Therefore, the new types of electrical-energy systems have received a resurgence of attention, such as sodium-ion batteries (SIBs) and potassium-ion batteries (PIBs), owing to similar electrochemical mechanism. Recently, the PIBs are considered as one of the most competitive candidates for large-scale energy storage systems, owing to its inherence of high energy density and economic efficiency, lower reduction potential of K^+/K (−2.93 V versus SHE) in a nonaqueous electrolyte, and the smallest Stokes radius of K-ions (3.6 Å in polycarbonate (PC). However, K-ion's large atomic radius (1.38 Å) and sluggish diffusivity lead to a great limitation for exhibiting excellent electrochemical performance. Recently, PIBs have been devised to optimize their electrochemical performances through various nanocomposite structures[1,2] and adjustments the composition of the electrolyte.[3,4]

An advanced flexible electrode (normally current collector-free flexible electrodes) not only notably reduces the total mass of electrodes, but also increases the energy density of cells that is critical to facilitate the development of wearable devices. Among numerous energy storage technologies, flexible batteries are considered as the most favorable candidate due to their high energy density, long cycle life, miniaturization, adaptability, and wearability are expected to be a part of such applications.[44,45,48,60,61] The traditional carbon-based materials were used as flexible substrates, such as carbon nanofibers, [5] soft carbon,[6,7] reduced graphene-oxide (rGO)[8] and other carbon series materials.[9] Compared to intercalated-type material (KC_8:<279 mAh g^{-1}), the alloyed or conversion-typed anode, especially chalcogenides,[10,11] phosphides[12] and alloy/de-alloy materials have high theoretical potassium-ion storage capacities with phosphorus by far upholding the highest capacity for PIBs (865 mAh g^{-1}).[13] Nevertheless, the poor rate performances and severe structural pulverization resulted from the intrinsic conductivity and huge volume expansion during charging/discharging process. As a result, it is a pivotal step to choose materials with high theoretical capacity and tough scaffold for anodes. Zhang *et al.* adopted the electrospinning approach to

* Corresponding author.
E-mail address: hytuan@che.nthu.edu.tw (H.-Y. Tuan).
[1] These authors contributed equally to this work.

https://doi.org/10.1016/j.cej.2020.127697
Received 25 August 2020; Received in revised form 1 November 2020; Accepted 8 November 2020
Available online 13 November 2020

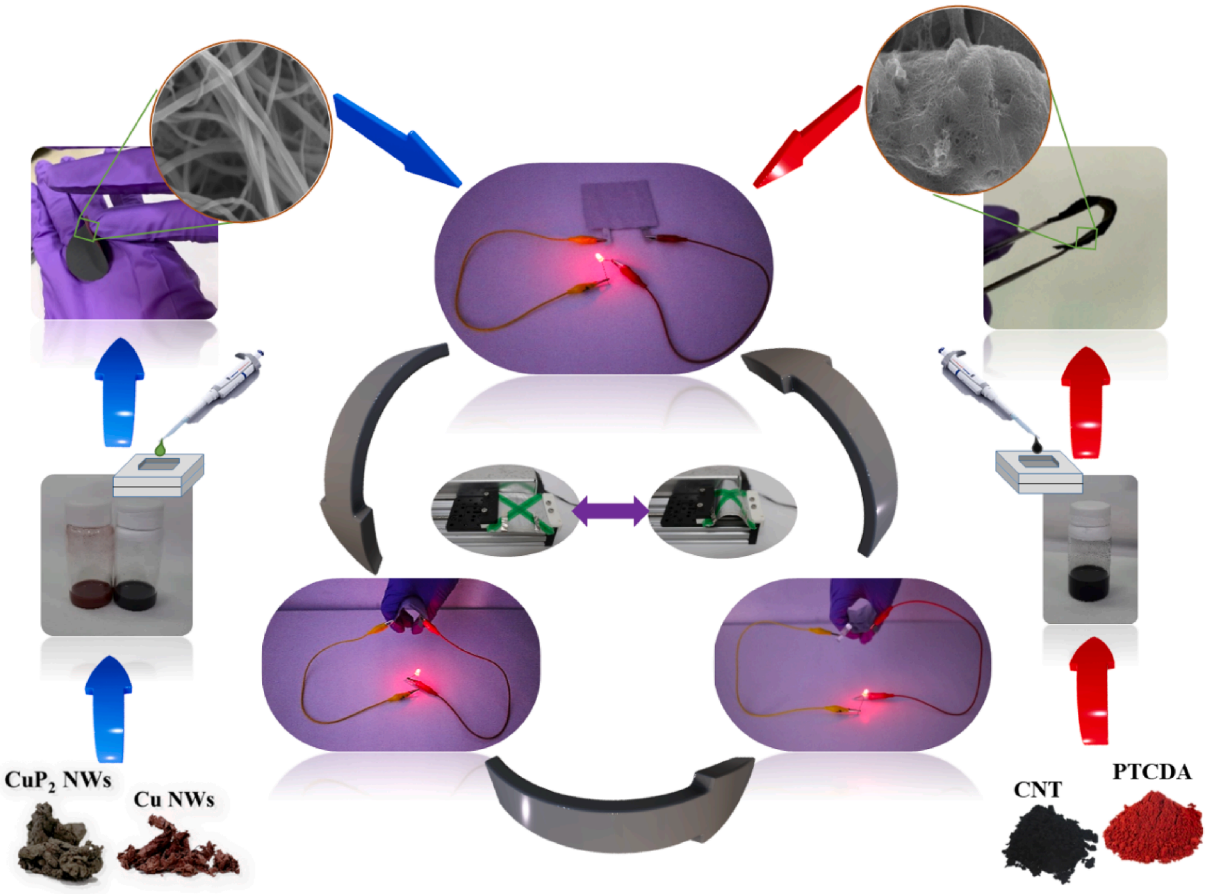

Fig. 1. Schematically illustration of the preparation and advantages of flexible and freestanding bilayer CuP_2/Cu NWs and PTCDA/CNT mesh electrodes.

fabricate $Co_{0.85}Se$ embedded in carbon nanofibers with one-step confined carbonization-selenidation process. This flexible and freestanding anode showed the high-rate capability because of surface-domination contribution.[11] Zhu *et al.* indicated that the enhanced non-Faradaic surface-controlled capacities can be attributed to the large electrolyte/electrode interface provided by the hollow nanostructure and porous network for highly favorable to obtain extraordinary high-rate performance.[12] Although most of them employ carbon framework to enable fast ion transfer and structural bendability for high-rate performance and flexible property, the highest current densities were still only 5 A g^{-1}. In addition, few reported literatures conducted the assemblies of full coin cells or pouch-typed batteries. The first high-energy pouch-typed PIBs were made up of the graphite and the crystalline Prussian blue (CTPB).[14] Nevertheless, the graphite is not a high mechanical material and its pouch-typed PIBs are not tested for long-cycle bending experiments.

While we are on the subject about full-cell research, it is also necessary for designing a suitable material as positive electrodes with excellent rate capability and pliable structure.[41] Zhu et al. devised a facile method of fabricating flexible binder-free electrodes via transformation of the corrosion layer of stainless-steel meshes into compact stack layers of Prussian blue nanocubes.[42] The perylene-3,4,9,10-tetracarboxylic dianhydride (PTCDA) is widely applied to the cathode material in sodium and lithium materials because of its stability and high specific capacity.[15,16] The poor conductivity of PTCDA, however, make it difficult for the transformation between C=O bonds and C-O-M (M: metal ion). Fortunately, Lu *et al.*[17] discovered that the electrochemical performance of PTCDA would be greatly improved after annealing at 450 °C and exhibits a capacity of 80 mAh g^{-1} at current density of 5000 mA g^{-1}. Moreover, Fei et al. demonstrated and all-solid-state potassium battery based on PTCDA and solid polymer electrolyte (SPE) [20]. Afterwards, several organic materials (e.g. PTCDI-DAQ[18] and PTCDI [19]) as a cathode were respectively reported.

However, it is still challenging to simultaneously high rate capability and ultra-stable open circuit potential (OCP) with flexible structure. In our work, a flexible nanostructured PIBs are demonstrated by taking advantage of bilayer-copper phosphide/copper nanowires (CuP_2/Cu NWs) mesh structure and the polymer-assisted assembly of PTCDA@-carbon nanotubes (CNTs). The bilayer-CuP_2/Cu NWs were synthesized by cross-winded properties of nanowires without binder and conductive agent. The preparation procedure of flexible anode and cathode have been schematically illustrated and depicted in Fig. 1. Both mesh electrodes were fabricated through layer-by-layer stacking and winding via a simple vacuum filtration method. The anode and cathode deliver remarkable capacities of 90 mA h g^{-1} at 12,000 mA g^{-1} and 113 mA h g^{-1} at 5250 mA g^{-1}, respectively. Furthermore, coin-typed full cell exhibits superior charging capacities of 117.3 mAh g^{-1} at 12,000 mA g^{-1} and the good retention (80% after 842 cycles at 400 mA g^{-1}). Upon the assembly of bilayer-CuP_2/Cu NWs-PTCDA@CNTs pouch-typed batteries, the extraordinary stability of structural tortuosity were confirmed by long-term bending test (5000 cycles), ultimately stimulating the pouch-type full battery could light up an LED brightly at different folding angles and also realize the freestanding and flexible features of anode and cathode. The excellent flexibility of pouch cells is based on two fundamental properties. Firstly, the CuP_2 NWs and Cu NWs individually intertwined which exhibit high mechanical strength through the Van deer Waals force. Secondary, the PTCDA contacted with CNTs results in the formation of a flexible nanocomposite film owing to the polymer-assisted assembling strategy. Both bilayer-CuP_2/Cu NWs anode and PTCDA@CNTs cathode could be easily curved as shown in the inset

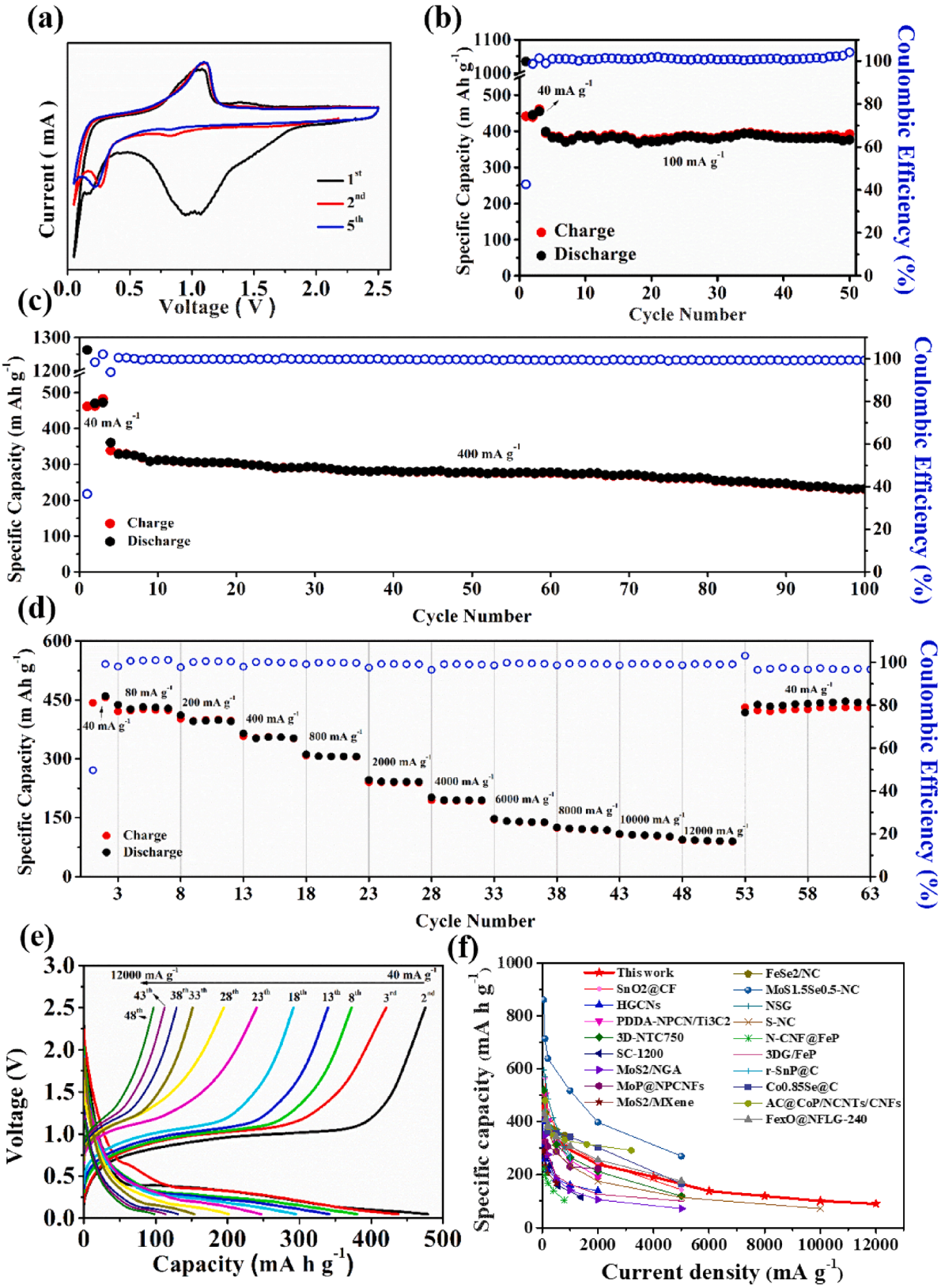

Fig. 2. Electrochemical performance of bilayer CuP_2/Cu nanowire mesh electrode: (a) cyclic voltammetry evaluation of bilayer CuP_2/Cu nanowire mesh electrode at a scan rate of 0.1 mV s^{-1}. (b) Cycling performance of bilayer CuP_2/Cu nanowire mesh electrode at the current density of 40 mA g^{-1} for first three cycles and 100 mA g^{-1} for other cycles. (c) Cycling performance of bilayer CuP_2/Cu nanowire mesh electrode at the current density of 40 mA g^{-1} for first three cycles and 400 mA g^{-1} for other cycles. (d) The rate performance of bilayer CuP_2/Cu nanowire mesh electrode at various rates from 40 mA g^{-1} to 12000 mA g^{-1} and (e) the corresponding voltage profile. (f) Rate performance of reported electrode materials for PIB system.[6,9,11,12,26–39]

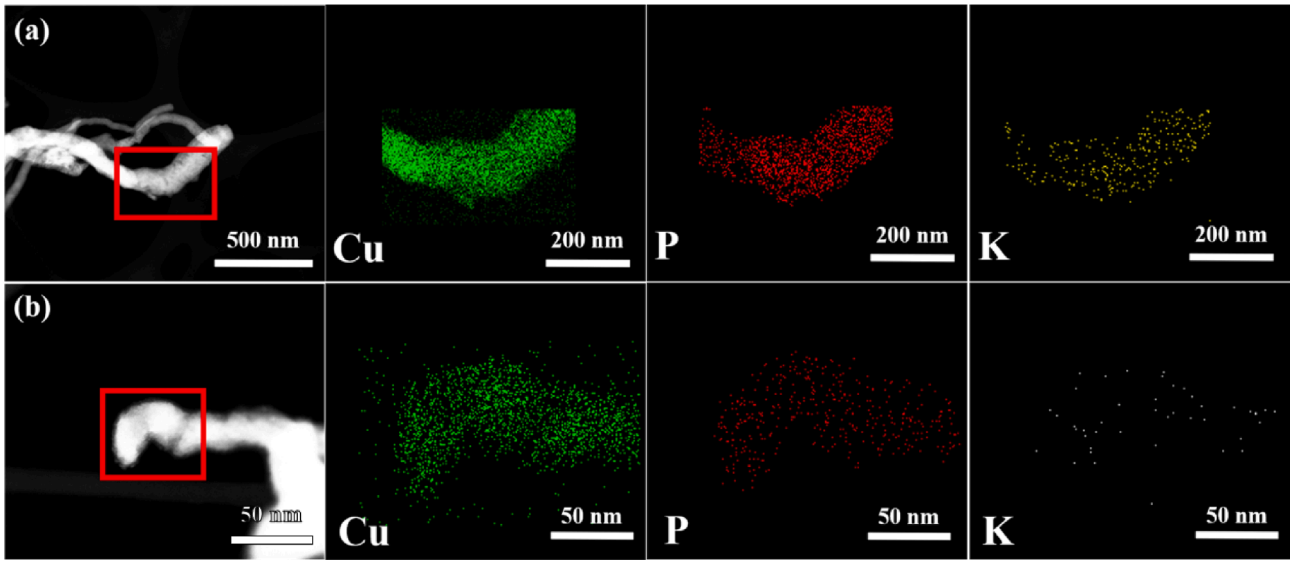

Fig. 3. Morphology and characterization of bilayer CuP_2/Cu nanowire mesh electrode after 10 cycles at 0.05 V and 2.5 V, respectively. (a) DF-STEM image of bilayer CuP_2/Cu nanowire mesh electrode at 0.05 V. EDS mapping images of Cu (green), P (red) and K (yellow) of CuP_2 nanowires. (b) DF-STEM image of bilayer CuP_2/Cu nanowire mesh electrode at 2.5 V. EDS mapping images of Cu (green), P (red) and K (yellow) of CuP_2 nanowires. (For interpretation of the references to colour in this figure legend, the reader is referred to the web version of this article.)

of Fig. 1. Given the advantages of mesh electrodes over common slurry system in PIBs, it is a promising candidate as a state-of-art flexible potassium-ion battery.

2. Results and discussion

The characterization and morphology of as-prepared CuP_2 are shown in **Figure S1**. The CuP_2 NWs has the crystalline monoclinic structure (lattice constants: a = 5.802 Å, b = 4.807 Å, c = 7.525 Å, and ß = 112.68°; JCPDS 65-1274) and no Cu_3P, Cu_2P_7 could be detected. Observed from low magnification scanning electron microscopy (SEM) image (**Figure S1(b)**), CuP_2 NWs are irregular wave-like shape and no obvious by-products. The consistent diameter of CuP_2 NWs, however, is about 30 nm revealed in high magnification SEM and TEM images (**Figures S1(c) and (d)**). Cu NWs were synthesized by a common hydrothermal method,[21] but there were a large amount of Cu nanoparticles (NPs) sticked on the nanowires. Hence, we separated the Cu NWs and Cu NPs by multiphase separation method.[22,23] The X-ray diffraction (XRD) pattern of purified Cu NWs with the typical face centered cubic (FCC) structure shows three distinct peaks at 2θ = 43.3, 50.5 and 74.1° assigned to the (1 1 1), (2 0 0) and (2 2 0) reflections of the Cu NWs.[24] On account of high-purity Cu NWs no characteristic peaks and images of Cu NPs could be seen (**Figures S2(a) and (b)**). As displayed in high magnification SEM and TEM image (**Figures S2(c) and (d)**), the ultra-consistent diameter of Cu NWs is about 50 nm. Because of the high aspect ratio of nanowire materials, it is suitable for the nanotechnology development of flexible electrodes.

The electrochemical performance of bilayer-CuP_2/Cu NWs mesh electrode was examined by a coin-type half cell with galvanostatic charge/discharge between 0.05 V and 2.5 V (vs. K/K^+), and the specific capacities was based on the mass of CuP_2 nanowires in this part. Besides, high-concertration KFSI in DME operates as the liquid electrolyte solution because of its capability of generating a more stable solid electrolyte interphase (SEI) and passivating the potassium foil in half cell.[7–9] Fig. 2 expressed the electrochemical performance of potassium half-cell (the corresponding voltage profiles were shown in **Figure S3**). Fig. 2**(a)** presents the cyclic voltammetry (CV) curves of the bilayer-CuP_2/Cu NWs mesh electrode for first few cycles. The cathodic peaks around 1.0 V in the initial cycle could be attributed to the irreversible reaction and conversion reaction for decomposition of the electrolyte and the formation of SEI layer, whereas other peaks around 0.3 V and 0.1 V are the electrochemical alloying process of CuP_2, as K^+ inserting into CuP_2 layer brought about reduction production. The anodic peak around 1.0 V was the electrochemical de-alloying process of CuP_2.[1,2] Afterwards, the overlap of the subsequent CV curves indicated reversible alloying/dealloying process for CuP_2 NWs. Fig. 2**(b)** showed that bilayer-CuP_2/Cu NWs mesh electrode exhibited a initial capacity of 441.3 mA h g^{-1} with 42.6% coulombic efficiency (CE) attributed to the irreversible reaction for the first cycle. After cycling at the current density of 40 mA g^{-1}, the bilayer-CuP_2/Cu NWs mesh electrode exhibited a specific charge capacity of 394 mA h g^{-1} at the current density of 100 mA g^{-1}. Furthermore, the bilayer CuP_2/Cu NWs mesh electrode maintained a specific charge capacity of 392 mA h g^{-1} with the retention of 99.5% after 50 cycles. Fig. 3**(a)** showed the dark field- scanning transmission electron microscopy (DF-STEM) and energy-dispersive X-ray spectroscopy (EDS) mapping images of the bilayer-CuP_2/Cu NWs mesh electrode after 10 cycles at 0.05 V, revealing that the Cu, P and K were distributed evenly in CuP_2 NWs during discharging process. Moreover, Fig. 3**(b)** showed the DF-STEM and EDS mapping images of the bilayer-CuP_2/Cu NWs mesh electrode after 10 cycles at 2.5 V, displaying the copper and phosphorous were still distributed evenly in CuP_2 NWs and the potassium scarcely could be seen during charging state, indicating that the alloy/de-alloy reaction of CuP_2 NWs could be conducted completely during potassiation and depotassiation process. Fig. 2**(c)** demonstrated the electrochemical performance of bilayer CuP_2/Cu NWs mesh electrode at high current density of 400 mA g^{-1}. The bilayer-CuP_2/Cu NWs mesh electrode remained a specific charge capacity of 230.4 mA h g^{-1}, representing that the retention of 70% after 100 cycles. **Figure S4** further exhibited the DF-STEM and EDS mapping images of bilayer-CuP_2/Cu NWs mesh electrode after 100 cycles, the structrue integrity was well maintained.

To interpret the outstanding rate capability of bilayer-CuP_2/Cu NWs anode, Fig. 2**(d,e)** exhibited that the rate performance, and it delivered the specific capacity of 456, 423, 397, 351, 305, 239, 192, 138, 119, 101 and 92 mA h g^{-1} at the current density of 40, 80, 200, 400, 800, 2000, 4000, 6000, 8000, 10,000 and 12,000 mA g^{-1}, respectively. When the current density was returned to 40 mA g^{-1}, the bilayer-CuP_2/Cu NWs mesh electrode still retained a high charge capacity of 440 mA h g^{-1}, corresponding to retention of 96.6% with respect to the 2nd cycle. The extraordinary rate capability and reversibility of bilayer-CuP_2/Cu NWs

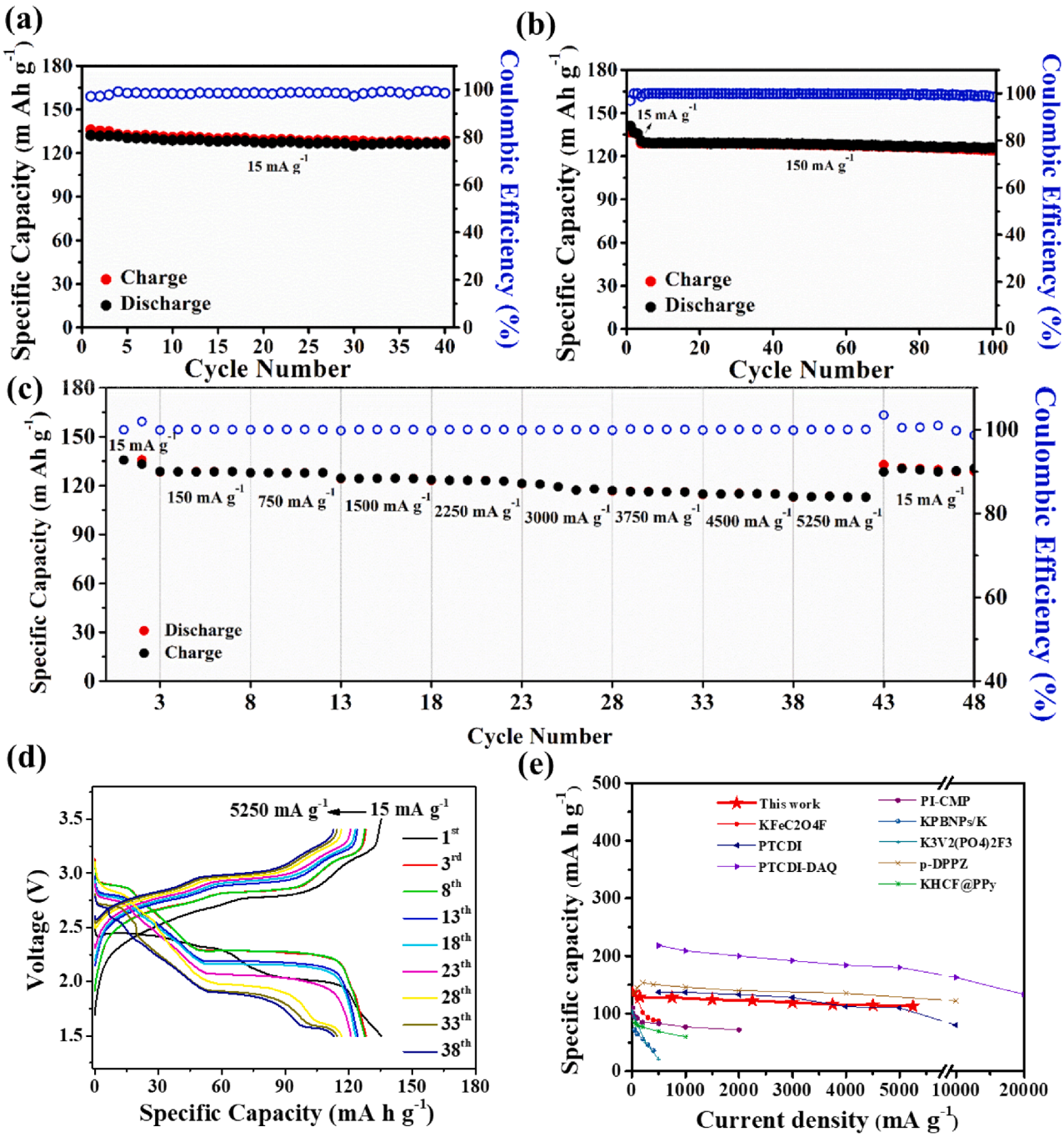

Fig. 4. Electrochemical performance of PTCDA film electrode: (a) Cycling performance of PTCDA film electrode at the current density of 15 mA g^{-1}. (b) Cycling performance of PTCDA film electrode at the current density of 15 mA g^{-1} for first three cycles and 150 mA g^{-1} for other cycles. (c) The rate performance of PTCDA film electrode at various current densities from 15 mA g^{-1} to 5250 mA g^{-1} and (d) the corresponding voltage profile. (e) Rate performance of reported electrode materials for PIB system.[18–20,43,46,47,49,50]

without any conductive additives was attributed to the bilayer nanowire interpenetrated structure.[25] In contrast with the literatures (Fig. 2**(f) and Table S1**),[6,9,11,12,26–39] the specific capacity of bilayer-CuP_2/Cu NWs mesh electrode at low current density is almost same as metal phosphide and lower than some metal sulfide or phosphorous/carbon composite. Surprisingly, the bilayer CuP_2/Cu NWs mesh electrode exhibited the best rate capability at ultra-high current density in any literatures.

Figure S5**(a)** presented that the SEM image of annealed PTCDA. In order to get the flexible cathode, we mixed CNTs, an ideal scaffold, with annealed PTCDA by poly(acrylic acid) (PAA).[40] As presented in Figure S5**(b)**, the film electrode which was peeled from filter membrane could be bent easily, indicating its great flexibility. Figures S5**(c) and (d)** showed that annealed PTCDA was perfectly covered by CNTs, forming a fine conductive network structure. Noticeably, the electrochemical performance of PTCDA@CNTs film electrode was tested by coin-typed half-cell with galvanostatic charge/discharge between 1.5 V and 3.5 V (vs. K/K^+) in potassium half-cell. The following capacities were calculated based on the mass of active PTCDA (60 wt% of all electrode) and the electrolyte solution was same as that of bilayer-CuP_2/Cu NWs mesh electrode. Fig. 4 expressed the electrochemical performance of PTCDA@CNTs film electrode in potassium half-cell, and the

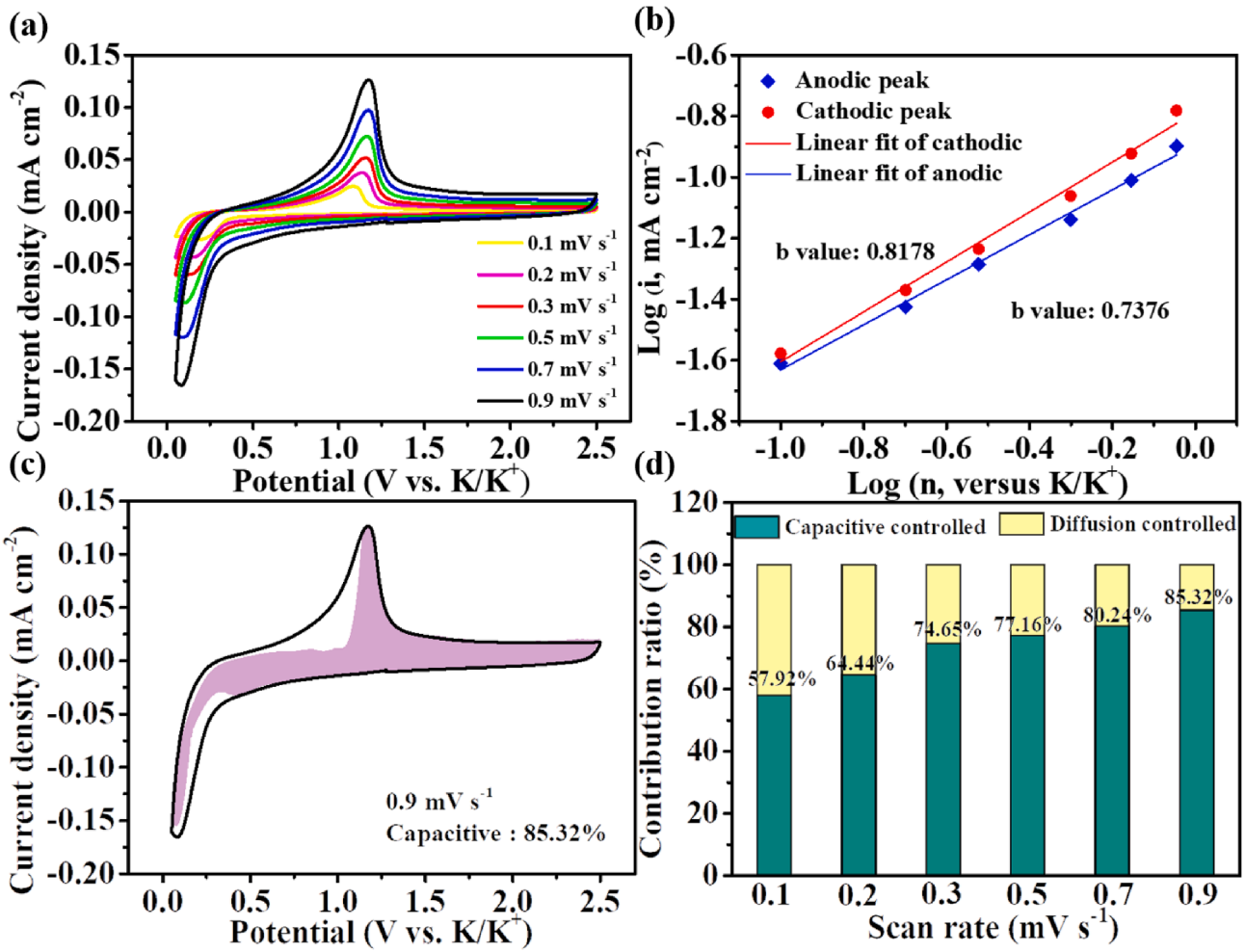

Fig. 5. Electrochemical analysis of kinetic behavior of the CuP_2/Cu NWs mesh electrode. (a) The cyclic voltammetry curves at various scan rate from 0.1 to 0.9 mV s^{-1}, (b) the corresponding log(i) as a function of log(ν) at the anodic and cathodic peak. (c) pseudocapacitive and diffusion-controlled condition at 0.9 mV s^{-1}, and normalized contribution ratio of surface kinetic and diffusive capacities at various scan rate from0.1 to 0.9 mV s^{-1}.

corresponding voltage profiles were attached in supporting information (**Figure S6**). Fig. 4**(a)** showed that PTCDA@CNTs film electrode at the low current density of 15 mA g^{-1}, exhibiting a specific discharge capacity of 132.2 mA h g^{-1} with high coulombic efficiency of 97.2% in the first cycle. After 40 cycles, the specific charge capacity still have 128.4 mA h g^{-1} with the retention of 97.1%. Fig. 4**(b)** demonstrated the electrochemical performance at high current density of 150 mA g^{-1}. After 100 cycles, the PTCDA@CNTs film electrode remained a specific charge capacity of 124.2 mA h g^{-1}, representing the retention of 96.2%. Fig. 4**(c) and (d)** exhibited the rate performance of the PTCDA@CNTs film electrode, which delivers the specific capacity of 135.7, 128.5, 127.9, 124.3, 122.7, 119.2, 116.1, 114.8 and 113 mA h g^{-1} at the current density of 15, 150, 750, 1500, 2250, 3000, 3750, 4500 and 5250 mA g^{-1}, respectively. When the current density was restored to 15 mA g^{-1} after 42 cycles of rate testing, the specific capacity of the PTCDA@CNTs film electrode returned to 132 mA h g^{-1} which was nearly equivalent to initially specific capacity. Evidently, the flexible and freestanding structure of PTCDA@CNTs film electrode compared to the traditional slurry system, exhibiting outstanding flexibility and the better electrochemical performance.[17] Furthermore, we also compared with reported literatures (Fig. 4**(e)**), [18–20,43,46,47,49,50] and then our cathode materials were much better than Prussian-blue and layered oxides analogs. In the organic materials series were on the top three compared with specific capacity as a function of current density.

In order to further explore electrochemical behaviors of bilayer-CuP_2/Cu NWs mesh and PTCDA@CNTs film electrodes, the K^+ insersion/extration kinetics were analyzed systematically by CV analysis. On the basis of CV curves of anode and cathode at various scan rate were shown in Figs. 5**(a) and** 6**(a)**, respectively. The relationship between the scan rate (ν) and peak current (I_p) could be expressed as the following formula:

$$I_p = a\nu^b$$

Normally, a *b*-value of 0.5 indicates an ideal diffustion-controlled electrochemical process, whereas the corresponding *b*-value of 1 demonstrates a kinetic surface-controlled step. The *b*-value presented in Figs. 5**(b) and** 6**(b)** could be acquired from plotting the log(ν) versus log (I_p), and here the b-value for anodic and cathodic peaks of bilayer-CuP_2/Cu NWs were 0.7376 and 0.8178, respectively. Also, the b-value for main anodic (a_2 : 0.8528) and cathodic (c_2 : 0.8193) peak of PTCDA@CNTs for PIBs have been obtained. The results indicated both CuP_2/Cu NWs and PTCDA/CNT film electrodes are a process dominated by surface kinetic-controlled. Moreover, the relationship between capacitive contribution factor ($k_2\nu$) and the supplementary diffusion contribution factor ($k_1\nu^{0.5}$) could be evaluated according to the following expression [26,51] :

$$I = k_1\nu^{0.5} + k_2\nu$$

After transformation, two parameters (k_1 and k_2) could be acquired by plotting the $I / \nu^{0.5}$ versus $\nu^{0.5}$. Based on this result of calculation, the contribution of surface kinetic reaction on bilayer-CuP_2/Cu NWs mesh

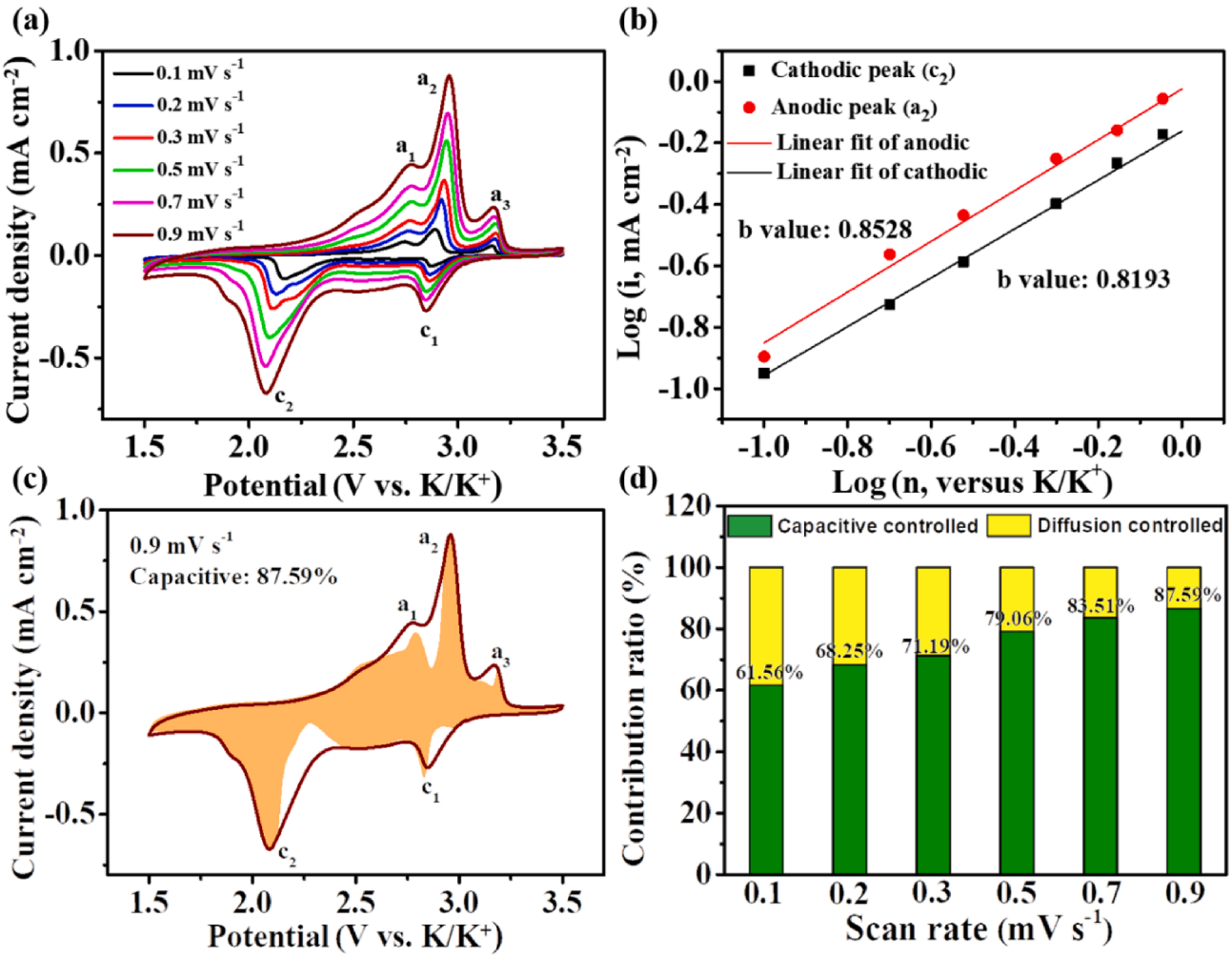

Fig. 6. Electrochemical analysis of kinetic behavior of the PTCDA/CNT mesh electrode. (a) The cyclic voltammetry curves at various scan rate from 0.1 to 0.9 mV s^{-1}, (b) the corresponding log(i) as a function of log(ν) at the anodic (a_2) and cathodic (c_2) peak. (c) pseudocapacitive and diffusion-controlled condition at 0.9 mV s^{-1}, and normalized contribution ratio of surface kinetic and diffusive capacities at various scan rate from0.1 to 0.9 mV s^{-1}.

and PTCDA@CNTs film electrodes were quantified of 85.32% and 87.59% at 0.9 mV s^{-1}, respectively, as exhibited in Figs. 5**(c) and** 6**(c)**. In addition, the capacitive contribution ratio could be augmented with the increase of sweeping speed (Figs. 5**(d) and** 6**(d)**), illustrating that the capacitive effect in high-current charging/discharging process should not be reckoned with. Evidently, the surface-dominated potassium-ion storage take place mainly on surface or near-surface zone during rapid potassiation, and could proceed with fast ion transfer, making it favorable for high rate capability. Moreover, surface-controlled storage can effectively avoid the cracking of structure because of the reduced K^+-insertion, enhancing the stability and cyclability. In the regard, self-intertwined nanowires or nanotubes promoted the pseudocapacitive-controlled system. Most importantly, the mesh electrodes with fluffy structure increase the interface between electrode and electrolyte, and then non-Faradaic reaction would be promoted during fast sweeping rate. Furthermore, the enhanced capacitive contribution is helpful effectively for improving the high-rate capacities responded to rechargeablility and reversibility under high current density. According to galvanostatic intermittent titration technique (GITT) analysis given in **Figures S7 and S8**, and the formula are listed in the following [52,53]:

$$D = \frac{4}{\pi\tau}\left[\frac{mV_m}{MS}\right]^2\left[\frac{\Delta E_s}{\Delta E_t}\right]^2 \approx \frac{4}{\pi\tau}[L]^2\left[\frac{\Delta E_s}{\Delta E_t}\right]^2$$

Note that the average thickness of electrodes was measured by cross-section SEM images given in Supporting information. The K^+ diffusion coefficient (D) of bilayer-CuP_2/Cu NWs mesh and PTCDA@CNTs film electrodes during the potassiation/depotassiation process were calculated to range from 10^{-11} to 10^{-13} cm^2 s^{-1} and from 10^{-9} to 10^{-13} cm^2 s^{-1}, separately. Notably, the diffusion coefficients of electrodes decreased sharply during the plateau potential of different state, with a voltage-dependent features since the alloying reaction of potassium-ion occured at the stage. Moreover, the diffusivity based on GITT results always assumed that it was a diffustion-controlled step for the potassium-ion transport in agreement with Fick's second law.[54] Therefore, we tested at quite slow current density (0.05C), meaning that the D value cannot always correspond to CV curves. Besides, we speculate that the de-alloying reaction could be conducted much easier than K^+-insertion reaction on the results of lower diffusion coefficient of plateau, thereby indicating a lower b-value of anodic peaks and non-negligable diffusion-controlled charging capacities.

To target a practical and desired potassium-ion module, the potassium metal were replaced with pre-potassiation host. That is, the potassium-ion full cells were fabricated by comprising an anode of bilayer-CuP_2/Cu NWs and a cathode of PTCDA@CNTs which were conducted respective pre-potassiation for 5 cycles before assembled. As shown in **Figure S9**, the simulation of charge curve of bilayer CuP_2/Cu NWs-PTCDA@CNTs full cell exhibits that the real charge curve of full cell should be located on 1.5 V to 3.5 V, which followed with three plateaus around at 2.3 V, 2.5 V and 2.9 V. Additionally, the simulation of discharge curve of full cell indicates that the real discharge curve of full

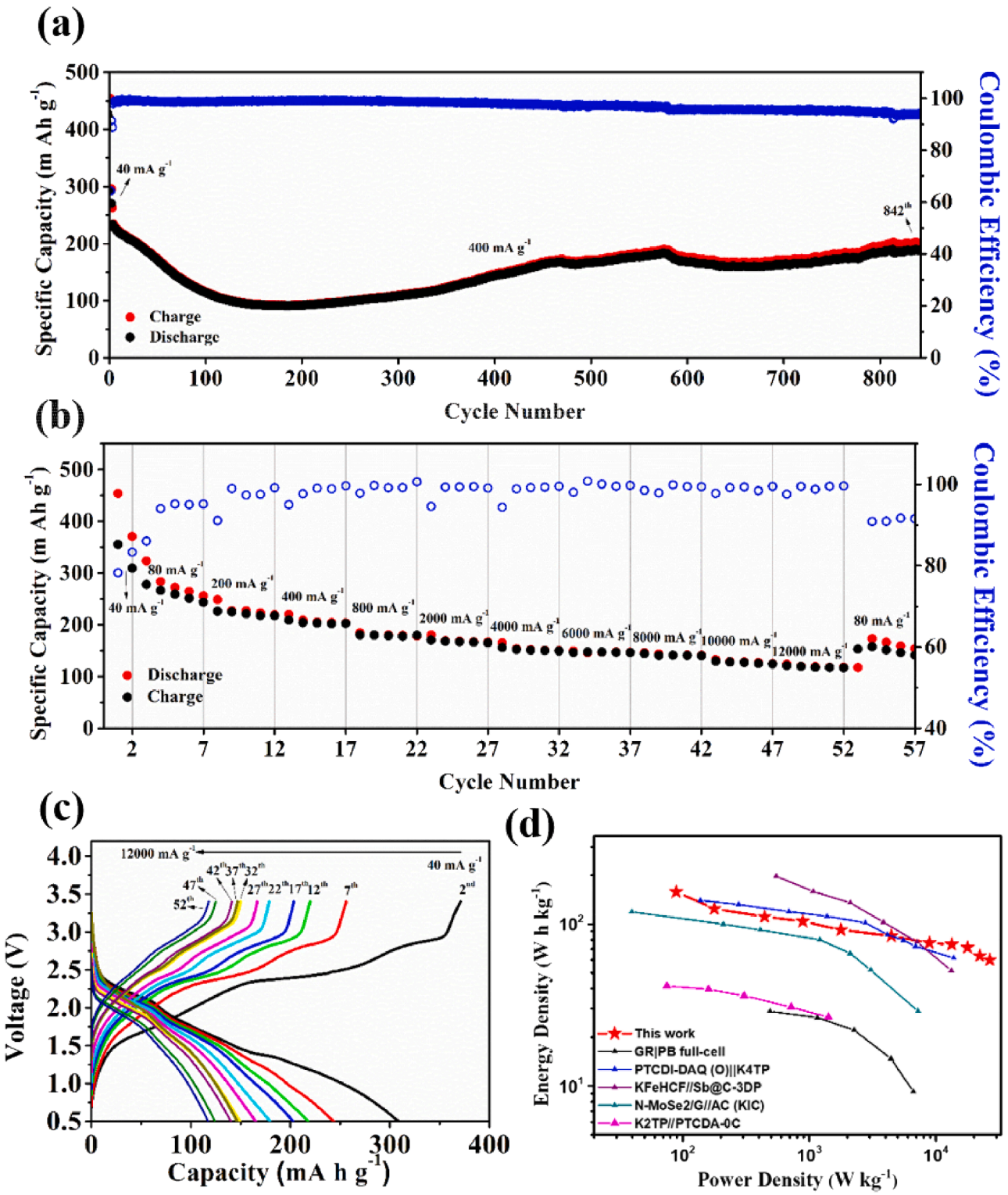

Fig. 7. Electrochemical performance of bilayer CuP_2/Cu NWs-PTCDA full-cell: (a) Cycling performance of bilayer CuP_2/Cu NWs-PTCDA coin full cell at the current density of 40 mA g^{-1} for first three cycles and 400 mA g-1 for other cycles. (b) The rate performance of bilayer CuP_2/Cu NWs-PTCDA coin full cell at various rates from 40 mA g-1 to 12000 mA g^{-1} and (c) the corresponding voltage profile. (d) Rate performance of reported electrode materials for PIB system based on total mass of electrodes [55–59].

cell should be located on 0.5 V to 2.5 V, which followed with two plateaus around at 1.4 V and 2.25 V. According to the results of the simulation of charge/ discharge curves, we operated the potential window of bilayer CuP_2/Cu NWs-PTCDA full-cell ranging from 0.5 V to 3.5 V. Fig. 7**(a)** showed that the bilayer CuP_2/Cu NWs-PTCDA@CNTs full-cell displayed a specific discharge capacity of 292 mA h g^{-1} with 64.3% Coulombic efficiency in the 1st (the corresponding voltage profile attached in supporting information). After 3 cycles at the current density of 40 mA g^{-1}, the bilayer-CuP_2/Cu NWs-PTCDA@CNTs full cell demonstrated that a specific charge capacity of 234 mA h g^{-1} at the

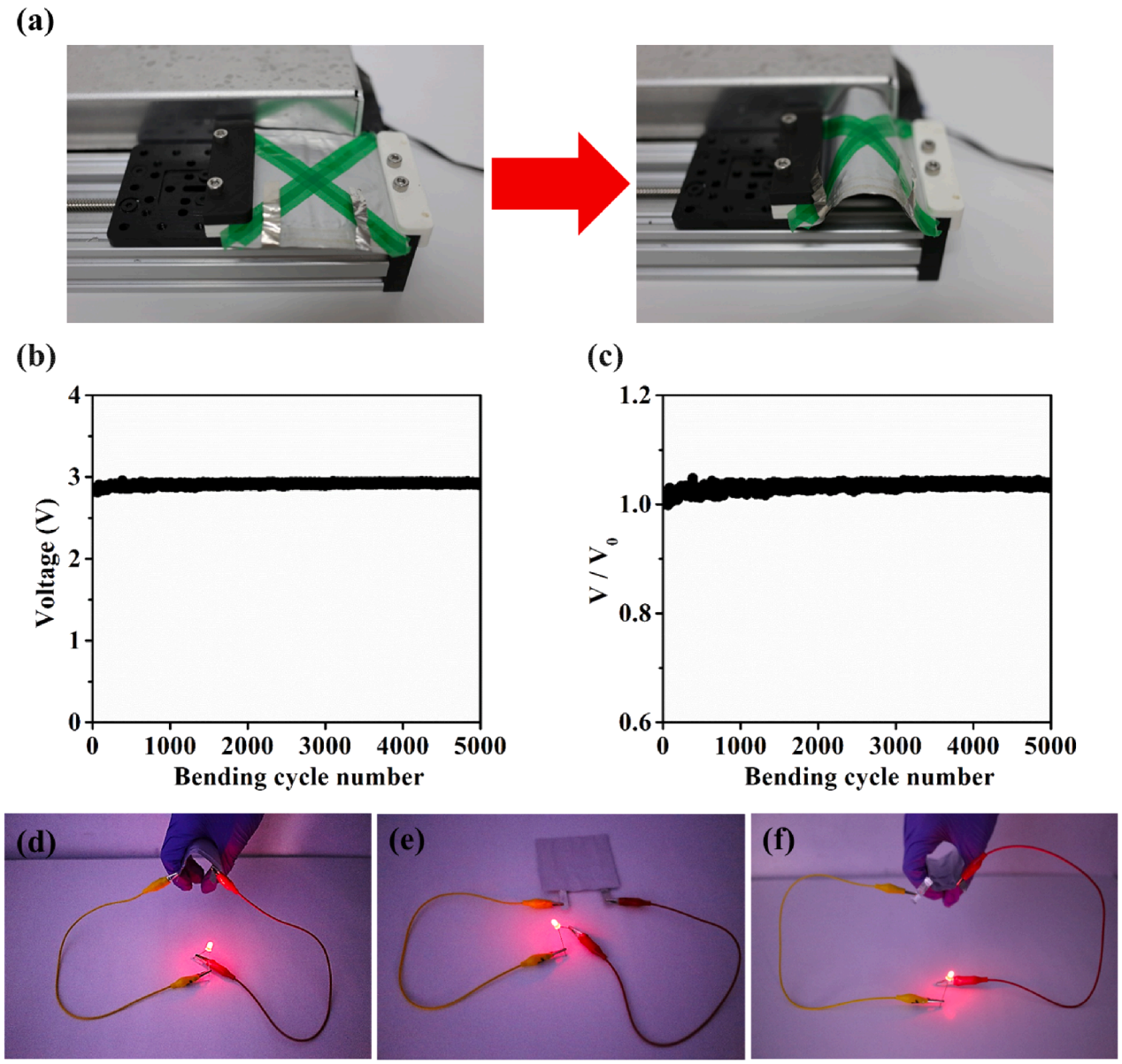

Fig. 8. The bending test of bilayer CuP_2/Cu NWs-PTCDA pouch type battery. (a) Schematic of bending test of pouch-typed full battery at a bending radius of 1.2 cm and the area of pouch-typed battery is 90 cm^2 (9 cm * 10 cm). (b, c) The voltage and normalized voltage record of pouch type full battery over 5000 bending cycles at a bending radius of 1.2 cm. (d, e, f) The photograph of pouch type full battery lighting up an LED under different bending and folding angles.

current density of 400 mA g^{-1}. Furthermore, the bilayer CuP_2/Cu NWs-PTCDA@CNTs full-cell remained 187 mA h g^{-1} with the high retention of about 80% after 842 cycles. It's worth noting that the rate performance of the bilayer-CuP_2/Cu NWs-PTCDA@CNTs full cell, which delivers the specific capacity of 309, 243, 217, 203, 179.7, 165.1, 149.3, 146.5, 140.2 124.2 and 117.3 mA h g^{-1} at the current density of 40, 80, 200, 400, 800, 2000, 4000, 6000, 8000, 10,000 and 1,2000 mA g^{-1}, respectively, shown in Fig. 7**(b)**. However, when the rate was restored to 80 mA g^{-1} after 53 cycles, the specific capacity of the bilayer-CuP_2/Cu NWs-PTCDA@CNTs full cell only returns to 157 mA h g^{-1}, corresponding to a low retention of 70.5% with respect to 13th cycle. This result may be attributed to the inequivalent decline of areal capacity of anode and cathode when the current density increasing. The outstanding electrochemical performance of the bilayer-CuP_2/Cu NWs-PTCDA@CNTs full-cell could be attributed to following: (i) Compared to the potassium foil, PTCDA@CNTs as a cathode which supply the source of potassium ions reduces the side effect in long-term cycle.[1] (ii) The excellent conductive network structure of anode and cathode leads to the full cell still work normally in super high current density. **Figure S11** showed that the anode and cathode electrodes which were disassembled after 842 cycles remained its integrity, indicating the structural stability that CuP_2 NWs and PTCDA were maintained a good contact with Cu NWs and CNTs, respectively. Most importantly, we also presented the Ragone plot in Fig. 7**(d)**,[18,55–59] and then the calculation of energy density and power density were determined from total weight of both electrodes.[18] Accordingly, the maxium energy densities for the full cells were estimated to be 685.7 Wh kg^{-1} (309 mAh g^{-1} × 2.22 V) for anode mass and 158.2 Wh kg^{-1} for total electrode mass. Meanwhile, a calculated high power density of 26630 W Kg^{-1} (117.3 mAh g^{-1} × 2.22 V @ 12 A g^{-1}) is also the best record among all K-ion full cells reported to date. The energy density of full cell have 76.4 Wh kg^{-1} at power density of 8876.9 W kg^{-1}. Even under the highest power density of 26,630 Wh kg^{-1}, the energy density still have 60.1 Wh kg^{-1}. Compared to other full cells, the performance of bilayer-CuP_2/Cu NWs-PTCDA@CNTs full cell was demonstrated stable and excellent energy density, especially at higher power density ranged from 8876.9 to

26630 W kg^{-1}.

To investigate the flexibility and safety of the full cells, we converted the coin-typed cell into pouch-typed battery. For a typical assembly of pouch-typed battery, both anode and cathode were pre-potassiated for 5 cycles in aluminum plastic film by using potassium foil as the counter electrode. After the pre-potassiation, the anode and cathode are reassembled with a new aluminum plastic film and charged to 3.5 V. Fig. 8 **(a)** displayed that the process of bending test of pouch-typed battery with a bending radius of 1.2 cm. It is worth noting that the the voltage and normalized voltage of the bilayer-CuP_2/Cu NWs-PTCDA@CNTs stabilizes at a constant value after 5000 bending cycles (Fig. 8**(b) and (c)**). The minor change of voltage results from the reduction of contact resistance when pouch-typed battery bending, and OCP stability enables a better utilization and safety. To fulfil battery application, we used the bilayer-CuP_2/Cu NWs-PTCDA@CNTs pouch-typed battery to light up an LED with different folding angles (Fig. 8**(d-f)**) and several LED lights (Figure S13). As a consequence, the performaces and configuration demonstrates a promising candidate that enables the PIBs to have the bendable architecture, prominent rate-capability, sufficient energy density at surpior power density, long shelf life and stable OCP during bending test to be an available option for the rechargeable battery system.

In summary, we successfully fabricated a flexible high-performance potassium battery by taking advantage of nanowires and nanotubes. Mesh electrodes exhibit pseudocapacitive domination under high current density owing to its fluffy structure. Therefore, the half-cell anode and cathode delivered a high reversible capacity and good rate capability. With the current collector-free design, the coin-typed full cell comprising a bilayer-CuP_2/Cu NWs anode and PTCDA@CNTs cathode give extraordinary rate performance and long cycling life (842 cycles). Surprisingly, the specific energy density under high power density region displayed the better rate-capabiltiy retention than reported literatures of potassium-ion full cells in the comparison plot based on the total mass of anode and cathode. It is worth noting that bilayer-CuP_2/Cu NWs-PTCDA@CNTs pouch-typed batteries obtained stable OCP during long-term bending test and lighted up an LED at different folding angles of pouch battery, revealing that this configuration is a promising option for sustainable battery systems.

Declaration of Competing Interest

The authors declare that they have no known competing financial interests or personal relationships that could have appeared to influence the work reported in this paper.

Acknowledgement

We acknowledge the financial support by the Ministry of Science and Technology through the grants of MOST 108-2636-E-007-013, MOST 108-2622-8-007-016, and MOST 109-2636-E-007-011 and by National Tsing Hua University, Taiwan through the grant of 107Q2708E1.

Appendix A. Supplementary data

Experimental details of material preparation; details on material and electrochemical characterization; SEM images, TEM images, XRD pattern, and electrochemical performance of CuP_2/Cu NWs and PTCDA@CNTs coin-typed half-cell; GITT results and diffusion coefficient of anode and cathode; images of disassembled coin full-cell corresponding to Figure 7(a); simulated charge-discharge curves of CuP_2/Cu NWs-PTCDA@CNTs full-cell. Supplementary data to this article can be found online at https://doi.org/10.1016/j.cej.2020.127697.

References

[1] W.C. Chang, J.H. Wu, K.T. Chen, H.Y. Tuan, Adv. Sci. 6 (2019) 1801354.
[2] P. Xiong, P. Bai, S. Tu, M. Cheng, J. Zhang, J. Sun, Y. Xu, Small (2018) e1802140.
[3] Q. Zhang, J. Mao, W.K. Pang, T. Zheng, V. Sencadas, Y. Chen, Y. Liu, Z. Guo, Adv. Energy Mater. (2018) 8.
[4] I.A. Shkrob, T.W. Marin, Y. Zhu, D.P. Abraham, J. Phys. Chem. C 118 (2014) 19661–19671.
[5] C. Shen, K. Yuan, T. Tian, M. Bai, J.-G. Wang, X. Li, K. Xie, Q.-G. Fu, B. Wei, ACS Appl. Mater. Interfaces 11 (2019) 5015–5021.
[6] Y. Liu, Y.X. Lu, Y.S. Xu, Q.S. Meng, J.C. Gao, Y.G. Sun, Y.S. Hu, B.B. Chang, C. T. Liu, A.M. Cao, Adv. Mater. 32 (2020) 2000505.
[7] C. Liu, N. Xiao, H. Li, Q. Dong, Y. Wang, H. Li, S. Wang, X. Zhang, J. Qiu, Chem. Eng. J. 382 (2020), 121759.
[8] S. Peng, L. Wang, Z. Zhu, K. Han, J. Phys. Condens. Matter 138 (2020), 109296.
[9] L. Tao, Y. Yang, H. Wang, Y. Zheng, H. Hao, W. Song, J. Shi, M. Huang, D. Mitlin, Energy Stor. Mater. 27 (2020) 212–225.
[10] G. Suo, J. Zhang, D. Li, Q. Yu, M. He, L. Feng, X. Hou, Y. Yang, X. Ye, L. Zhang, J. Colloid Interface Sci. 566 (2020) 427–433.
[11] C.A. Etogo, H. Huang, H. Hong, G. Liu, L. Zhang, Energy Stor. Mater. 24 (2020) 167–176.
[12] Z. Zhang, C. Wu, Z. Chen, H. Li, H. Cao, X. Luo, Z. Fang, Y. Zhu, J. Mater. Chem. A 8 (2020) 3369–3378.
[13] W. Zhang, J. Mao, S. Li, Z. Chen, Z. Guo, J. Am. Chem. Soc. 139 (2017) 3316–3319.
[14] Y.-H. Zhu, X. Yang, D. Bao, X.-F. Bie, T. Sun, S. Wang, Y.-S. Jiang, X.-B. Zhang, J.-M. Yan, Q. Jiang, Joule 2 (2018) 736–746.
[15] J. Manuel, X. Zhao, K.-K. Cho, J.-K. Kim, J.-H. Ahn, ACS Sustainable Chem. Eng. 6 (2018) 8159–8166.
[16] C. Yuan, Q. Wu, Q. Shao, Q. Li, B. Gao, Q. Duan, H.G. Wang, J. Colloid Interface Sci. 517 (2018) 72–79.
[17] L. Fan, R. Ma, J. Wang, H. Yang, B. Lu, Adv. Mater. 30 (2018), e1805486.
[18] Y. Hu, W. Tang, Q. Yu, X. Wang, W. Liu, J. Hu, C. Fan, Adv. Funct. Mater. 30 (2020) 2000675.
[19] M. Xiong, W. Tang, B. Cao, C. Yang, C. Fan, J. Mater. Chem. A 7 (2019) 20127–20131.
[20] H. Fei, Y. Liu, Y. An, X. Xu, G. Zeng, Y. Tian, J. Feng, J. Power Sources 399 (2018) 294–298.
[21] Y. Zhang, J. Guo, D. Xu, Y. Sun, F. Yan, Langmuir 34 (2018) 3884–3893.
[22] F. Qian, P.C. Lan, T. Olson, C. Zhu, E.B. Duoss, C.M. Spadaccini, T.Y. Han, Chem. Commun. 52 (2016) 11627–11630.
[23] C. Kang, S. Yang, M. Tan, C. Wei, Q. Liu, J. Fang, G. Liu, ACS Appl. Nano Mater. 1 (2018) 3155–3163.
[24] T.-H. Duong, H.-C. Kim, Ind. Eng. Chem. Res. 57 (2018) 3076–3082.
[25] W.-C. Chang, T.-L. Kao, Y. Lin, H.-Y. Tuan, J. Mater. Chem. A 5 (2017) 22662–22671.
[26] J. Li, B. Rui, W. Wei, P. Nie, L. Chang, Z. Le, M. Liu, H. Wang, L. Wang, X. Zhang, J. Power Sources 449 (2020), 227481.
[27] Z. Li, N. Sun, R. Soomro, Z. Guan, L. Ma, M. Jiang, Q. Zhu, B. Xu, ACS Nano (2020).
[28] W. Miao, X. Zhao, R. Wang, Y. Liu, L. Li, Z. Zhang, W. Zhang, J. Colloid Interface Sci. 556 (2019) 432–440.
[29] H. Qiu, L. Zhao, M. Asif, X. Huang, T. Tang, W. Li, T. Zhang, T. Shen, Y. Hou, Energy Environ. Sci. 13 (2020) 571–578.
[30] Q. Tan, P. Li, K. Han, Z. Liu, Y. Li, W. Zhao, D. He, F. An, M. Qin, X. Qu, J. Mater. Chem. A 7 (2019) 744–754.
[31] X. Wang, J. Ma, J. Wang, X. Li, J. Alloys Compd 821 (2020), 153268.
[32] C. Yang, Y. Li, F. Zheng, Y. Li, Q. Deng, W. Zhong, G. Wang, T. Liu, Chem. Eng. J. (2020), 124590.
[33] R. Zhao, H. Di, X. Hui, D. Zhao, R. Wang, C. Wang, L. Yin, Energy Environ. Sci. 13 (2020) 246–257.
[34] Z. Yi, Y. Liu, Y. Li, L. Zhou, Z. Wang, J. Zhang, H. Cheng, Z. Lu, Small 16 (2020) 1905301.
[35] W. Zhang, J. Yin, M. Sun, W. Wang, C. Chen, M. Altunkaya, A.H. Emwas, Y. Han, U. Schwingenschlögl, H.N. Alshareef, Adv. Mater. (2020) 2000732.
[36] J. Chu, Q. Yu, K. Han, L. Xing, Y. Bao, W.A. Wang, Carbon 161 (2020) 834–841.
[37] X. Dong, Z. Xing, G. Zheng, X. Gao, H. Hong, Z. Ju, Q. Zhuang, Electrochim. Acta 339 (2020), 135932.
[38] H.N. Fan, X.Y. Wang, H.B. Yu, Q.F. Gu, S.L. Chen, Z. Liu, X.H. Chen, W.B. Luo, H. K. Liu, Adv. Energy Mater. 10 (2020) 1904162.
[39] B. Li, S. Shang, J. Zhao, D.M. Itkis, X. Jiao, C. Zhang, Z.-K. Liu, J. Song, Carbon (2020).
[40] Y. Cheng, Z. Chen, M. Zhu, Y. Lu, Adv. Energy Mater. (2015) 5.
[41] Y. Zhu, X. Yang, T. Sun, et al., Electrochem. Energ. Rev. 1 (2018) 548–566.
[42] Y.H. Zhu, Y.B. Yin, X. Yang, T. Sun, S. Wang, Y.S. Jiang, X.B. Zhang, Angew. Chem. Int. Ed. Engl. 129 (2017) 7989–7993.
[43] B. Ji, W. Yao, Y. Zheng, P. Kidkhunthod, X. Zhou, S. Tunmee, S. Sattayaporn, H.-M. Cheng, H. He, Y. Tang, Nat. Commun. 11 (2020) 1–10.
[44] Y.H. Zhu, X.Y. Yang, T. Liu, X.B. Zhang, Flexible 1D batteries: recent progress and prospects, Adv. Mater. 32 (2020) 1901961.
[45] T. Liu, Y. Yu, X.Y. Yang, J. Wang, X.B. Zhang, Small Struct. (2020) 2000015.
[46] X. Lin, J. Huang, H. Tan, J. Huang, B. Zhang, Energy Stor. Mater. 16 (2019) 97–101.
[47] F.A. Obrezkov, V. Ramezankhani, I. Zhidkov, V.F. Traven, E.Z. Kurmaev, K. J. Stevenson, P.A. Troshin, J. Phys. Chem. Lett. 10 (2019) 5440–5445.
[48] X.Y. Yang, X.L. Feng, X. Jin, M.Z. Shao, B.L. Yan, J.M. Yan, Y. Zhang, X.B. Zhang, Angew. Chem. Int. Ed. Engl. 58 (2019) 16411–16415.
[49] Q. Xue, L. Li, Y. Huang, R. Huang, F. Wu, R. Chen, ACS Appl. Mater. Interfaces 11 (2019) 22339–22345.
[50] C. Zhang, Y. Xu, M. Zhou, L. Liang, H. Dong, M. Wu, Y. Yang, Y. Lei, Adv. Funct. Mater. 27 (2017) 1604307.

[51] K. Yao, Z. Xu, M. Ma, J. Li, F. Lu, J. Huang, Adv. Funct. Mater. (2020) 2001484.
[52] S. Dong, D. Yu, J. Yang, L. Jiang, J. Wang, L. Cheng, Y. Zhou, H. Yue, H. Wang, L. Guo, Adv. Mater. (2020) 1908027.
[53] X. Hu, G. Zhong, J. Li, Y. Liu, J. Yuan, J. Chen, H. Zhan, Z. Wen, Energy Environ. Sci. (2020).
[54] L. Qin, N. Xiao, J. Zheng, Y. Lei, D. Zhai, Y. Wu, Adv. Energy Mater. 9 (2019) 1902618.
[55] X.-D. He, Z.-H. Liu, J.-Y. Liao, X. Ding, Q. Hu, L.-N. Xiao, S. Wang, C.-H. Chen, J. Mater. Chem. A 7 (2019) 9629–9637.
[56] K. Moyer, J. Donohue, N. Ramanna, A.P. Cohn, N. Muralidharan, J. Eaves, C. L. Pint, Nanoscale 10 (2018) 13335–13342.
[57] W. Qiu, H. Xiao, Y. Li, X. Lu, Y. Tong, Small 15 (2019) 1901285.
[58] Z. Tong, S. Tian, H. Wang, D. Shen, R. Yang, C.S. Lee, Adv. Funct. Mater. 30 (2020) 1907656.
[59] Y. Yi, Z. Sun, C. Li, Z. Tian, C. Lu, Y. Shao, J. Li, J. Sun, Z. Liu, Adv. Funct. Mater. 30 (2020) 1903878.
[60] T. Liu, X.L. Feng, X. Jin, M.Z. Shao, Y.T. Su, Y. Zhang, X.B. Zhang, Angew. Chem. Int. Ed. Engl. 58 (2019) 18240–18245.
[61] Y.H. Zhu, Q. Zhang, X. Yang, E.Y. Zhao, T. Sun, X.B. Zhang, S. Wang, X.Q. Yu, J. M. Yan, Q. Jiang, Chemistry 5 (2018) 168–179.